Interfacial charge carrier dynamics of cuprous oxide-reduced graphene oxide (Cu$_2$O-rGO) nanoheterostructures and their related visible-light-driven photocatalysis

Ying-Chih Pu [a],[*],[1], Hsin-Ying Chou [b],[1], Wen-Shuo Kuo [c],[d], Kung-Hwa Wei [b], Yung-Jung Hsu [b],[*]

[a] Department of Materials Science, National University of Tainan, Tainan 70005, Taiwan
[b] Department of Materials Science and Engineering, National Chiao Tung University, Hsinchu 30010, Taiwan
[c] Advanced Optoelectronic Technology Center, National Cheng Kung University, Tainan 701, Taiwan
[d] Center for Micro/Nano Science and Technology, National Cheng Kung University, Tainan 701, Taiwan

ARTICLE INFO

ABSTRACT

We demonstrated a facile and green preparation of cuprous oxide-reduced graphene oxide (Cu$_2$O-rGO) nanoheterostructures through a photochemical reaction. The density of Cu$_2$O nanocubes (NCs) grown on the rGO surface can be well controlled by modulating the concentration of GO employed in the reaction. Because of the relatively low potential of Fermi level of rGO, the photoexcited electrons on the conduction band (CB) of Cu$_2$O NCs preferentially transfer to rGO, simultaneously leaving photogenerated holes on the valence band (VB) of Cu$_2$O, resulting in the notable charge carrier separation properties. Time-resolved photoluminescence (TRPL) spectra were collected to quantitatively analyze the electron transfer rate constant (k_{et}) between Cu$_2$O NCs and rGO, and the dependence of the k_{et} on the rGO constituent in Cu$_2$O-rGO nanoheterostructures. Among all the samples tested, the Cu$_2$O-rGO nanoheterostructure with the rGO constituent of 2 wt.% (denoted as Cu$_2$O-rGO-2) displayed the largest k_{et} as well as the most pronounced charge separation property. The optimized Cu$_2$O-rGO-2 showed the best methyl orange (MO) photocatalytic degradation performance, which was highly consistent with the trend of the obtained k_{et} results. As compared with relevant commercial products, such as N-doped P-25 TiO$_2$ and commercial Cu$_2$O powders, the Cu$_2$O-rGO-2 exhibited superior efficiency toward MO degradation under visible light illumination, illustrating its potential for applications in relevant photoelectric conversion processes. The recycling trial showed that the Cu$_2$O-rGO-2 has promising potential for use in the long-term course of photocatalysis to degrade organic pollutants. Furthermore, the photocatalytic efficiency evaluated under natural sunlight demonstrated that the present Cu$_2$O-rGO nanoheterostructure could effectively harvest the energy of solar spectrum and converted it into the chemical energy for organic pollutants degradation. The current study could provide great insights into the design of semiconductor/graphene composites which exhibit remarkable charge separation properties for practical applications in the organic pollutants photodegradation, solar fuel generation as well as photovoltaic devices.

© 2016 Elsevier B.V. All rights reserved.

1. Introduction

Graphene is a single atomic layer of graphite and possesses the two-dimensional (2D) sp^2-bonded carbon network [1,2], which is different from 1D carbon nanotubes [3] and 3D ball-like C$_{60}$ [4]. In addition, graphene has attracted enormous scientific interest because of its extremely high electron mobility of 2×10^5 cm^2 V^{-1} s^{-1} [5,6], tremendous specific surface area of ~2965 m^2 g^{-1} [7], and remarkable thermal and chemical stability [5,6,8–11]. These unique properties make graphene a promising additive or supporting component for potential applications in numerous fields, including transistors [12–14], sensors [15–17], fuel cells [18–20], lithium ion batteries [21–23], supercapacitors [24–27], and solar energy conversions [28–31]. One particular interest among the applications is the demonstration of photoelectric conversion by using semiconductor-graphene

nanoheterostructures (SGNs) [32–34]. As a result of the unique properties of graphene, the SGNs exhibit an effective charge separation performance, leading to the enhancement in the efficiency of photoelectric or energy conversion [35–39]. For example, CdS clusters showed a significant enhancement in photocatalytic hydrogen production when they were deposited on graphene nanosheets [35]. This enhancement was mainly attributed to the supported graphene which could serve as an effective electron scavenger to capture the photoexcited electrons from the conduction band (CB) of CdS to perform water reduction and generate hydrogen. Similarly, the photocatalytic activity of ternary nanocomposite photoelectrodes composed of CdS nanocrystallites, reduced graphene oxide (rGO), and TiO_2 nanotube (TNT) array had been investigated in visible-light-driven photoelectrochemical hydrogen production [36]. The middle layer of rGO not only played as electron transfer mediator for suppressing the charge carrier recombination, but also served as a photosensitizer to increase the photon capture ability for improving the photocatalytic activity. On the other hand, the TiO_2-graphene acted as a superior electron collection layer in $CH_3NH_3PbI_{3-x}Cl_x$ perovskite solar cell to improve the power conversion efficiency (PCE) up to 15.6% as compared to the 10.0% PCE of $CH_3NH_3PbI_{3-x}Cl_x$ perovskite solar cell without using graphene [37]. The enhancement was mainly due to the reduction of the series resistance and lower recombination rate in the perovskite solar cell by employing graphene at the interface. To date, various types of SGNs have been proposed and fabricated to further the advancement of photoelectric conversion technologies under visible light illumination [38,40–42]. However, the potential toxic issue of cadmium or lead toward organisms and environment limits the development for these visible light activated photocatalysts [43]. The nontoxic and bio-friendly SGNs are still needed for practical utilization in the energy harvesting from natural sunlight.

The most common composition of the environment- or bio-friendly SGN is TiO_2-graphene, which displays great performance in the applications of photocatalytic pollutant decomposition or water splitting, as well as photovoltaics [44–48]. However, the intrinsic large band gap (3.0–3.2 eV) limits the photon capture ability of TiO_2 from natural sunlight [49–52]. On the other hand, as an abundant element and nontoxic semiconductor, with a band gap of ~2.0 eV, cuprous oxide (Cu_2O) has emerged as a great solar absorber for diverse photoelectric conversion applications in the visible spectrum [53–55]. Furthermore, recent efforts have focused on the fabrication of Cu_2O-graphene nanoheterostructure to develop a promising visible-light-driven photocatalyst to produce solar fuel or achieve organic pollutant degradation [56–61]. An and co-workers reported that the optimized Cu_2O-rGO composite could achieve activity six times higher than pure Cu_2O and 50 times higher than Cu_2O-RuO_x for the CO_2 photoreduction [59]. The improvement of the photoactivity was mainly contributed by the efficient charge separation in Cu_2O-rGO composite. The Cu_2O-rGO composites with optimal rGO contents have demonstrated enhanced visible photocatalytic activity [62,63]. Tran et al. have reported that Cu_2O-rGO composite could significantly enhance the photocatalytic activity and stability of Cu_2O for H_2 generation because of the increased charge separation efficiency and the efficient charge transportation at the interface [60]. The effect of the crystal facets of Cu_2O-rGO composite on the photocatalytic degradation of organic pollutant under visible light illumination has been studied by Zou et al. [61]. The results indicated that the unsaturated Cu on Cu_2O {111} facets could generate the strong interaction with rGO, which benefits the rapidly photo-generated electron transfer from Cu_2O to rGO to improve the photoactivity. Furthermore, the essential role of the defects of rGO in enhancing the photocatalytic efficiency of Cu_2O-rGO has also been revealed [65]. Despite the previous intense studies on Cu_2O-rGO composites, the fundamental understanding of interfacial charge carrier dynamics and their correspondence to the resultant photocatalytic properties are still lacking.

Therefore, examination of interfacial charge-carrier dynamics in SGNs is critical, which could establish the correlation between the exciton transfer or relaxation processes and the performance of photoelectric conversion, as well as photocatalytic pollutant degradation [64–69]. For instance, Lightcap et al. reported that the rate constants for the electron transfer at the interface of CdSe quantum dot (QD) and GO composite can reach as high as $6.7 \times 10^8\,s^{-1}$ [70]. By virtue of the ultrafast interfacial electron transfer, the CdSe-graphene composite showed improved photocurrent response (~150%) over pure CdSe photoelectrode. Besides, the interfacial charge carrier dynamics for three components semiconductor-metal-semiconductor, $Na_xH_{2-x}Ti_3O_7$-Au-Cu_2O, Z-scheme nanoheterosture has been demonstrated [71]. The investigation revealed that the change of shell thickness of Cu_2O could modulate the energy band structure and the related interfacial charge carrier transfer rate, which in turn affected the performance in photocatalytic dye decomposition. Furthermore, the ultrafast exciton and charge-carrier dynamics in InGaN/GaN nanowires with and without the decoration of catalyst, Rh/Cr_2O_3 nanoparticle (NP) have been studied [72]. As compared to bare InGaN/GaN nanowires, Rh/Cr_2O_3 nanoparticles decorated InGaN/GaN nanowires showed an additional exciton relaxation pathway within a time constant of 50 ps, which could be attributed to the interfacial charge transfer of photoexcited electrons from the CB of InGaN/GaN to Rh/Cr_2O_3 nanoparticle, resulting in the superior photocatalystic water splitting [73]. However, there are very few studies in the literature about the charge carrier dynamics of Cu_2O-graphene nanoheterostructures and their correlation with the resultant photoelectric conversion efficiency has never been reported. A quantitative study on this subject is thus essential and important to the fundamental understanding as well as the practical applications for Cu_2O-graphene nanoheterostructures.

In this work, we presented the study of interfacial charge carrier dynamics for Cu_2O-rGO heterostructure system. The samples were prepared by depositing cubical Cu_2O nanocrystals (NCs) on the surface of rGO sheets using a facile and green photochemical reduction process at room temperature without any strong reduce agent. With the good control of the ratio between the precursor of Cu_2O and the employed GO in the photochemical process, the decorated density of Cu_2O NCs on rGO sheets can be readily controlled. Characterization of the structural and optical properties of the obtained Cu_2O-rGO samples were accomplished by scanning and transmission electron microscopies (SEM and TEM), X-ray diffraction (XRD), Fourier transform infrared (FT-IR), Raman, and UV–vis spectra. Time-resolved photoluminescence (TRPL) measurements were conducted to explore the interfacial charge carrier dynamics for the as-prepared Cu_2O-rGO nanoheterostructures. By probing the emission lifetime of an indicator dye, (9-anthracene carboxylic acid, 9ACA), the electron transfer events between Cu_2O nanocube and rGO sheet were quantitatively analyzed. The results of charge carrier dynamics gained from Cu_2O-rGO nanoheterostructures can be well correlated to their photoconversion efficiency evaluations in dye (methyl orange, MO) degradation under visible light illumination. Furthermore, the investigation of the photodegradation mechanism revealed that the radical anion ($^\bullet O_2^-$) served as a critical role to dominate the MO degradation. The remarkable electron collector, rGO, and the superior charge separation property contributed to the superior photocatalytic efficiency observed for the optimized Cu_2O-rGO nanoheterostructure. The results of recycling trials and the natural sunlight illumination of MO photodegradation demonstrated the great potential of Cu_2O-rGO nanoheterostructure for the practical applications in the solar energy conversion.

2. Experimental

2.1. Preparation of GO

GO was prepared using the typical Hummers' method, including the graphite oxidation and the subsequent exfoliation [39,74].

2.2. Preparation of pristine Cu_2O NCs

First, 30 mg of cupric acetate ($Cu(OAc)_2$) was dissolved in 20 mL of a mixed solution that contained ethylene glycol ($C_2H_6O_2$, EG) and deionized (DI) water with a volume ratio of 3:1. Afterwards, 0.25 mL of an aqueous 0.05 M polyethylene glycol (PEG, Mw = 600) solution was added to the above solution, and the mixture was kept in the dark with an N_2 purge for 30 min. The subsequent 4 h of UV irradiation (λ = 254 nm, 32 W) with an N_2 purge for the mixed solution led to the growth of Cu_2O nanocrystals. The product was collected by centrifugation, washed with ethanol and DI water, and then dried in vacuum for later use.

2.3. Preparation of Cu_2O-rGO nanoheterostructures

The same photochemical reduction method was used for the preparation of Cu_2O-rGO nanoheterostructures. 30 mg of $Cu(OAc)_2$ was first dissolved in 20 mL of a mixed solution that contained EG and DI water in a volume ratio of 3:1. Afterwards, 0.25 mL of an aqueous 0.05 M PEG (Mw = 600) solution was added to the above mixture. The GO powder from Hummer's method was then added into the mixed solutions with the desired amount of 0.075 mg (0.25 wt.% relative to $Cu(OAc)_2$), 0.15 mg (0.5 wt.%), 0.3 mg (1 wt.%), 0.6 mg (2 wt.%), 1.5 mg (5 wt.%) and 3 mg (10 wt.%), respectively. After 30 min of ultrasonication, the above mixtures were stirred and purged with N_2 in the dark for another 30 min. Subsequently, 12 h of UV irradiation (λ = 254 nm, 32 W) with an N_2 purge was applied to produce Cu_2O-rGO nanoheterostructures. The products were collected by centrifugation, washed with ethanol and DI water, and then dried in vacuum for later used. On the other hand, the bare rGO sheet without Cu_2O NC decoration was prepared using the same procedure without adding $Cu(OAc)_2$ and PEG solutions.

2.4. Photocatalytic activity measurement

The photocatalytic performance of the Cu_2O-rGO nanoheterostructures was evaluated by monitoring the photodegradation of MO under xenon lamp irradiation (500 W, light intensity of 175 mW/cm^2) with a bandpass filter of 400–700 nm at room temperature. A 20 mL quartz tube was used as the photoreactor vessel. The photodegradation of MO in the presence of five types of photocatalysts, which included N-doped TiO_2, bare rGO sheets, Cu_2O NCs, Cu_2O@rGO (i.e., a physical mixture of Cu_2O NCs and rGO sheets) and Cu_2O-rGO nanoheterostructures was evaluated. A typical experiment involved adding 4 mg of photocatalyst to 20 mL of aqueous MO solution (5.0×10^{-5} M) in the photoreactor vessel. Prior to irradiation, the suspension was stirred in the dark for 30 min to reach the adsorption equilibrium. At various time intervals throughout the irradiation, 1 mL aliquots of the reaction solution were withdrawn and centrifuged to remove the photocatalyst. A UV–vis spectrum of the filtrate was then acquired to measure the concentration variation of MO by recording the absorbance of the characteristic peak at 464 nm. To investigate the chemical stability of Cu_2O-rGO nanostructure, three cycles of photocatalytic reactions were performed. For the recycling test, the sample was collected by centrifugation after 120 min of reaction. The residual catalyst was washed with DI water and ethanol and then used for the next run of reaction. The photodegradation of MO under natural sunlight in the presence of

the Cu_2O-rGO nanoheterostructures was also examined. The total organic carbon (TOC) content of MO was also recorded to ensure the degraded MO was certainly decomposed.

2.5. Characterizations

The morphology and dimensions of the Cu_2O-rGO nanoheterostructures were examined using a high-resolution transmission electron microscope (HRTEM, JEOL JEM-3000) operated at 300 kV and a field-emission scanning electron microscope (FESEM JSE-6500F). XRD patterns were measured on a Shimadzu XRD6000 with Cu Kα radiation (λ = 1.54056 Å) at a rate of 4° per minute in 2θ over a range of 10° to 80°. Raman measurements were performed using a Horiba Jobin Yvon HR800 microscope and a Raman spectroscope equipped with a liquid nitrogen-cooled charge-coupled device detector. The Raman excitation wavelength of 632.8 nm was provided by a 20 mW He-Ne laser. The FT-IR spectra were recorded by a Perkin-Elmer FT-IR spectrometer. UV–vis spectra were collected with a Hitachi U-3900H spectrophotometer at room temperature under ambient conditions. The zeta-potential data were obtained using a Zetasizer Nano ZS90 (Malvern), which measured the electrophoretic mobility of the sample and derived the zeta-potential value from the Smoluchowski equation. TRPL spectra were measured using a time correlated single-photon counting system (Pico Quant GmbH) which used a 375 nm picosecond pulsed laser diode (PDL-800-B, 20 MHz) as the excitation source. The TOC content of MO was determined by a Shimadzu TOC-LCPH analyzer.

3. Results and discussion

3.1. Structural investigation of Cu_2O-rGO nanoheterostructures

In this work, GO and cupper precursor ($Cu(OAc)_2$) were used as raw materials to synthesize Cu_2O-rGO nanoheterostructures by a photochemical reduction process under UV irradiation of 254 nm at room temperature. Since Cu^{2+} can bind to the functional groups of GO ($-COOH$, $-OH$, $-O-$ or sp^2 carbons) through Coulombic interaction (electrostatic attraction) [75,76], the GO sheet can be reduced into rGO accompanied with Cu_2O nanocrystals (NCs) formation on its surface after a fixed period of UV irradiation. Fig. 1 shows the information that elucidates the composition and structure of the target materials. Fig. 1(a) includes an SEM image of the monodisperse cubical like Cu_2O NCs with an average edge length of approximately 500 nm; these Cu_2O NCs were prepared using the photoreduction process without the incorporation of GO sheets. The TEM image in the inset of Fig. 1(a) clearly shows that the Cu_2O NCs were well-defined cubic structure with the uniform sharp edges. Fig. 1(b) represents the SEM and TEM images (inset) of Cu_2O-rGO nanoheterostructures, which demonstrates that the Cu_2O NCs were monodispersively grown on the rGO surface without any agglomeration by using present photoreduction process. The magnified TEM image of Cu_2O-rGO nanoheterostructure in Fig. 1(c) shows that the Cu_2O NCs were in direct contact with the surface of the rGO sheet. The square region of the Cu_2O-rGO nanoheterostructure in Fig. 1(c) is magnified and shown as the inset. The lattice fringes of Cu_2O NCs were clear and the interlayer spacings of 0.30 nm were measured, which is consistent with the lattice spacing of the (110) lattice of cubic-phase Cu_2O [77]. The composition of the Cu_2O-rGO nanoheterostructure was then examined using TEM-EDS. The results of the elemental mapping of C, Cu and O were shown in Fig. 1(d), which confirmed the composition of the observed cubical Cu_2O NCs on the rGO sheets.

The corresponding XRD pattern of the GO, Cu_2O NCs and Cu_2O-rGO nanoheterostructures are shown in Fig. 1(e). The GO exhibited
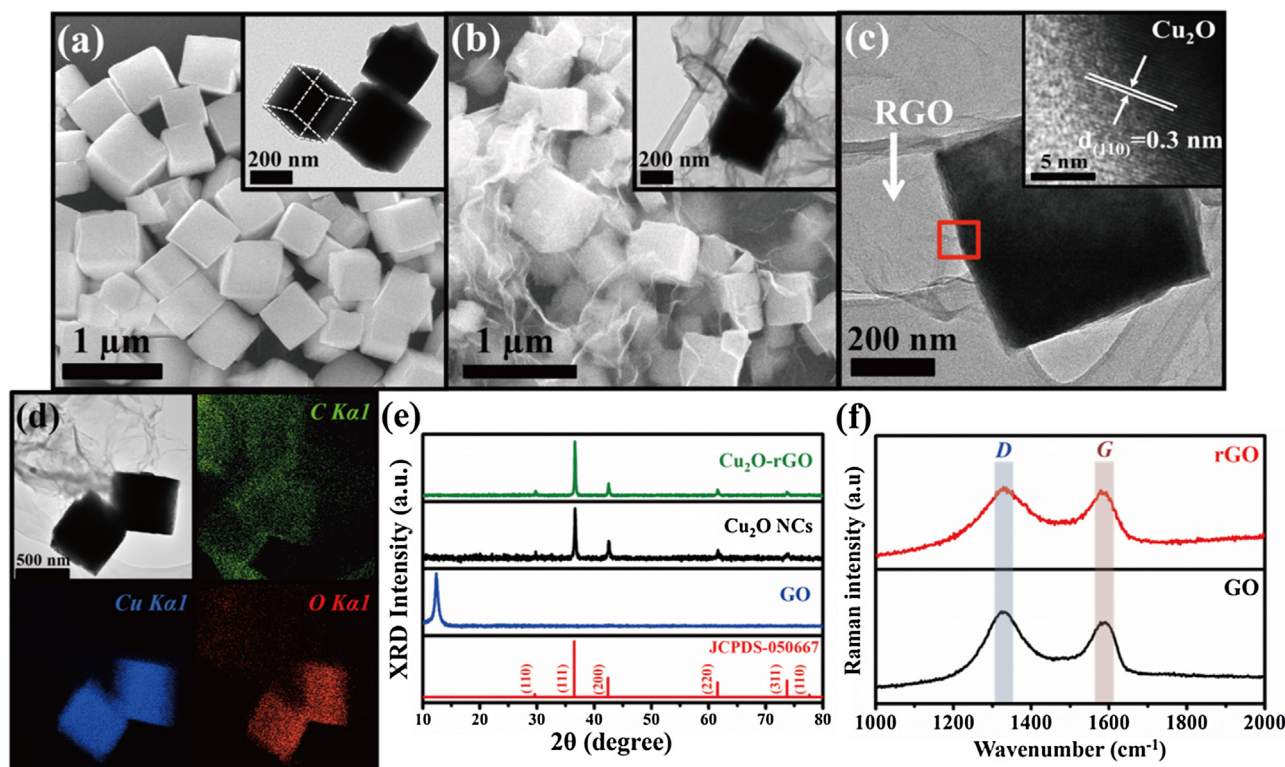
Fig. 1. (a) SEM and TEM images of Cu_2O NCs. (b) SEM and TEM images of Cu_2O-rGO nanoheterostructures. (c) HRTEM image of Cu_2O-rGO nanoheterostructures and the inset shows the lattice fringes at the marked red region. (d) TEM-EDS elemental mapping of Cu_2O-rGO nanoheterostructures. (e) XRD patterns for GO, Cu_2O NCs and Cu_2O-rGO nanoheterostructures. The pattern of the reference cubic phase Cu_2O was also included for comparison. (f) Raman spectra of GO and rGO sheets. (For interpretation of the references to colour in this figure legend, the reader is referred to the web version of this article.)
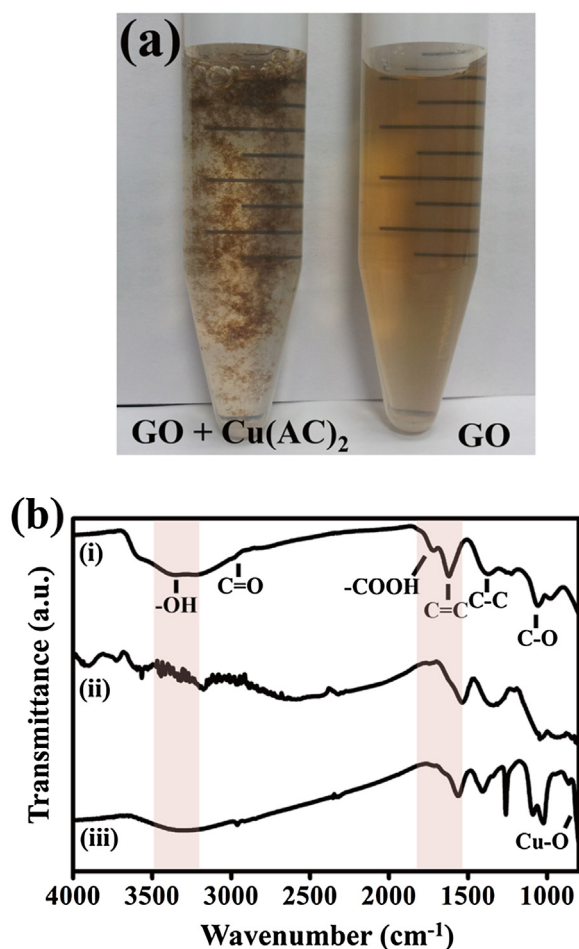
a peak at $2\theta = 12.4°$, which corresponds to the reported value of the interlayer spacing of GO (0.71 nm). The XRD peaks of Cu_2O NCs that was obtained by the photoreduction process can be indicated as the cubic-phase Cu_2O by referring to the standard pattern of JCPDS-050667. For Cu_2O-rGO nanoheterostructures, the characteristic peaks of GO were absent, which illustrates that the present photosynthesis process can successively reduce GO to produce rGO. To further confirm the chemical state of rGO, the samples were characterized by Raman measurements and the results were shown in Fig. 1(f). The relative intensity between peak at $\sim 1350\,cm^{-1}$ (D band) and $\sim 1580\,cm^{-1}$ (G band) provides significant information for evaluating the transformation from GO to rGO. Usually, the D band can be attributed to a breathing mode of k-point phonons with A_{1g} symmetry, which represents the contribution of local defects and disorder, while the G band is attributed to E_{2g} phonon of sp^2 C=C [78]. Consequently, the intensity ratio of the characteristic peaks (I_D/I_G) can be used to estimate the graphitic property of carbon materials [79]. Here, after photochemical reduction, the values of I_D/I_G of GO were reduced from 1.20 to 1.06. The decrease of the I_D/I_G value indicates that the GO sheets were transformed into graphitic rGO, which demonstrates that the present photochemical process is a facile and effective method to reduce the local defects or disordered structures from oxygenated functional groups on GO, and further produce the sp^2 C=C structures to form rGO. This result, together with the findings of the TEM, XRD and EDS analyses, confirms that the present one-step photochemical reduction process can successfully produce the desired Cu_2O-rGO nanoheterostructures.

3.2. Growth mechanism of Cu_2O-rGO nanoheterostructures

When $Cu(OAc)_2$ was added to the GO suspension solution, the clear, brown-colored solution rapidly turned into a dark brown

precipitate as a result of the formation of $Cu(OAc)_2$-GO complex as shown in Fig. 2(a). We collected the dark brown precipitate by centrifugation, washing and then redispersed it in DI water for zeta-potential measurements. The zeta-potential characterization showed that the GO sheets exhibited a negative surface charge, -21.1 mV; however, the $Cu(OAc)_2$-GO complex displayed a dramatically positive charge of $+0.1$ mV. The variation of surface charge indicated that the $Cu(OAc)_2$ adsorbed on the oxygenated groups of GO sheet, thus changing the surface charge from negative to positive. In order to confirm the interaction between $Cu(OAc)_2$ and GO, the FT-IR spectra of GO, $Cu(OAc)_2$-GO, and CuO-rGO were collected as shown in Fig. 2(b). A broad peak at $3400\,cm^{-1}$ and a peak at $1050\,cm^{-1}$ could be indicated as the hydroxyl groups (-OH) and the epoxy groups (C—O) of GO, respectively. The peaks at 2860 and $1730\,cm^{-1}$ were corresponded to the C=O bending vibrations and stretching vibrations of carboxyl group. The C—C and C=C bending vibrations at 1420 and $1629\,cm^{-1}$ were also observed. All of these signals suggest the presence of a high density of oxygenated groups of the as-prepared GO, which is consisted with Zhou's study [75]. As the $Cu(OAc)_2$ was mixed with GO, the broad signal of hydroxyl group disappeared and the signal of carboxyl group showed the apparent shift to lower wavenumber, which demonstrated the strong interaction between $Cu(OAc)_2$ and the surface function groups of GO [76]. After the photochemical reaction for $Cu(OAc)_2$-GO complexes, the peak of C=C skeletal vibration of graphene and peak of Cu-O vibration of Cu_2O at 1589 and $630\,cm^{-1}$ were observed in Fig. 2(c), which confirmed the formation of rGO and Cu_2O [58]. The results of zeta-potential and FT-IR measurements reveal that the $Cu(OAc)_2$ can easily bind to GO, forming $Cu(OAc)_2$-GO complexes to benefit the formation of Cu_2O-rGO nanoheterostructure during the photochemical reduction.

The possible growth mechanism of Cu_2O and rGO from $Cu(OAc)_2$ and GO under UV light irradiation can be proposed as follows.

Fig. 2. (a) Photograph of GO solution and GO solution mixed with Cu(OAc)₂. (b) FT-IR spectra of (i) GO, (ii) GO—Cu(OAc)₂ and (iii) Cu₂O-rGO nanoheterostructures.

the Cu(OAc)₂-GO complexes, the intramolecular transfer of photoexcited electrons from the π-system of the carboxylate to the Cu^{2+} (ligand-to-metal charge-transfer, LMCT) under UV light irradiation can take place, which has been proposed in Long's study [82]. Briefly, upon light irradiation Cu(OAc)₂ was transformed into an intermediate CuOOCCH₃ and then undergo decarboxylation to form methyl copper (CH₃Cu, Cu(I)). Subsequently, the CH₃Cu can react with H_2O to produce Cu_2O nucleus, followed by the growth of Cu_2O nanocrystals capped with PEG. Because of the intense chemical binding between Cu(OAc)₂ and GO, the Cu_2O NCs can *in-situ* growth on the rGO sheets to form the homogeneous Cu_2O-rGO nanoheterostructures.

3.3. Controlling the decoration density of Cu₂O NCs on rGO sheets

By controlling the relative amount of the precursors, Cu(OAc)₂ and GO, we were able to modulate the decoration density of the Cu_2O NCs on the surface of rGO sheets. Fig. 3(a–f) represents the SEM images of the Cu_2O-rGO nanoheterostructures with gradual increase in the loading amount of GO as 0.25, 0.5, 1, 2, 5 and 10 wt.% in the mixed solutions, respectively. The thus-obtained samples were denoted as Cu_2O-rGO-0.25, Cu_2O-rGO-0.5, Cu_2O-rGO-1, Cu_2O-rGO-2, Cu_2O-rGO-5 and Cu_2O-rGO-10, respectively. Obviously, the decoration density of Cu_2O NCs was decreased with the increasing of the rGO constituent. The microstructures of the samples were further examined with TEM observations as shown in Fig. 3(g–l). Not that the rGO-free sheets or free-standing Cu_2O NCs were rarely observed in the products, demonstrating the advantage of the current facile and green approach for obtaining the homogeneous and decoration density-tunable Cu_2O-rGO nanoheterostructures. Importantly, the controllable decoration density may affect the optical properties and interfacial charge transfer behavior of Cu_2O-rGO nanoheterostructures, which will be further discussed later.

3.4. Optical properties of Cu₂O NCs and Cu₂O-rGO nanoheterostructures

The optical properties of Cu_2O NCs and Cu_2O-rGO nanoheterostructures were characterized by UV–vis absorption spectroscopy. As shown in Fig. 4, all the samples displayed significant light absorption in the visible range of 500–700 nm. The Cu_2O NCs showed the corresponding excitonic band gap absorption around 620 nm ($\sim$2.0 eV). For the Cu_2O-rGO nanoheterostructures, the absorption intensity at the visible range was substantially enhanced, which became increasingly pronounced as increasing the component of rGO. This outcome was majorly due to the

During the UV irradiation (λ = 254 nm), the π-π^* excitation of the electrons in sp² domains of the GO would generate photoexcited electron and hole. The electron can move to the epoxy groups for C—O—C bond breaking (photoreduction). The C—O bonds of GO are destroyed during the photoreduction, resulting in the consequentially O_2 releasing and further form the SP² π-conjugated rGO [78,80]. On the other hand, the solvent, EG, is a kind of alcohol in the mixed solution, which could serve as a hole scavenger to capture the photoexcited holes from GO [52,81]. In the meantime, for
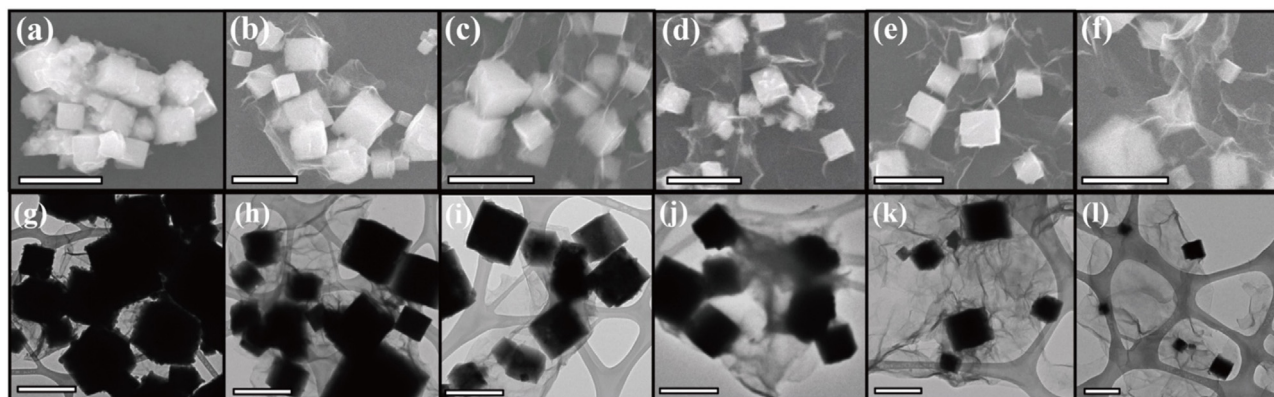

Fig. 3. (a–f) SEM and (g–l) TEM images of the as-prepared Cu₂O-rGO nanoheterostructures. (a, g) Cu₂O-rGO-0.25, (b, h) Cu₂O-rGO-0.5, (c, i) Cu₂O-rGO-1, (d, j) Cu₂O-rGO-2, (e, k) Cu₂O-rGO-5 and (f, l) Cu₂O-rGO-10. The scale bars of SEM and TEM are 1 μm and 500 nm, respectively.

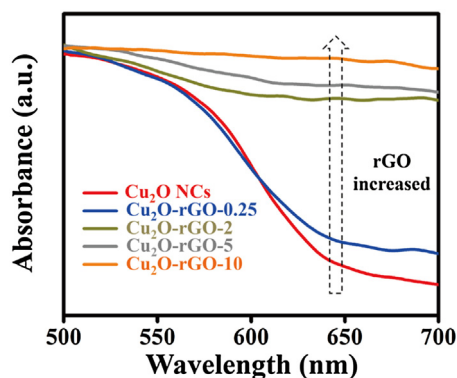**Fig. 4.** UV–vis absorption spectra of the Cu_2O NCs and Cu_2O-rGO nanoheterostructures.

micron-meter size of rGO which induced significant light scattering during the measurement and thus increased the photon capture ability of Cu_2O NCs in Cu_2O-rGO nanoheterostructures [59]. The apparent enhancement of the visible light absorption ability of Cu_2O-rGO nanoheterostructures make them a promising candidates for solar-driven photocatalysis applications. Before the practical using in the application of photoelectric conversion, the investigation of interfacial charge carrier dynamics is essential for us to gain the insights to optimize the composition of Cu_2O-rGO nanoheterostructures.

3.5. Charge carrier dynamics of Cu_2O-rGO nanoheterostructures

In this work, an indicator dye, 9ACA, was used to monitor the charge carrier dynamics of the Cu_2O-rGO nanoheterostructures. 9ACA has been widely utilized to bind with TiO_2 to form dye-sensitized semiconductor electrodes and investigate their interfacial electron transfer dynamics [83–85]. In this study, 9ACA is employed as a probe molecule to adsorb on the surface of Cu_2O-rGO nanoheterostructures, which provides informative PL signals, such as PL intensity and exciton lifetime at 460 nm, to characterize their interfacial charge transfer dynamics. Fig. 5(a) shows the steady-state PL spectra of 9ACA in different experimental conditions. The PL intensity of 9ACA showed a decay behavior when the Cu_2O NCs and rGO were dispersed in the 9ACA solution, respectively (sample was denoted as 9ACA/Cu_2O and 9ACA/rGO). The PL intensity decay became more pronounced as the Cu_2O-rGO nanoheterostructures (Cu_2O-rGO-2) were introduced in 9ACA solution. Note that when 9ACA contacted with the Cu_2O NCs or Cu_2O-rGO nanoheterostructures, it did not undergo photocatalysis to decompose during the short time period of the PL measurement (within 20 s). Fig. 5(b) shows the comparison of the TRPL spectra of 9ACA under the above experimental conditions. The emission decay of pure 9ACA can be fit with a double-exponential decay kinetics, generating a fast decay component of 43.3% with a 2.53 ns (τ_1) and 56.7% of slow decay component with a lifetime of 4.99 ns (τ_2). Upon the introduction of Cu_2O NCs, the fast and slow decay components of 9ACA were reduced to 2.06 ns with an enhanced amplitude of 50.7% and 4.79 ns with a decreased amplitude of 50.3%, respectively. This result illustrates that the appearance of additional nonradiative pathway from the electronic interaction between 9ACA and Cu_2O. As the Cu_2O-rGO nanoheterostructures with different constituent of rGO (samples were denoted as 9ACA/Cu_2O-rGO-x, x were 0.25, 0.5, 1, 2, 5, 10) were introduced, the TRPL profiles of 9ACA also followed the double-exponential decays but represented the faster decay than 9ACA/Cu_2O. In order to further compare the PL decay behavior of 9ACA as it contacted with the different samples, the

intensity-average lifetime was calculated by the following equation:

$$\langle \tau \rangle = \left(A_1 \tau_1{}^2 + A_2 \tau_2{}^2 \right) / \left(A_1 \tau_1 + A_2 \tau_2 \right)$$

The fitting and calculation results of the PL decay of 9ACA in different experimental conditions are listed in Table 1. The average PL lifetimes were obtained as 4.29 ns for 9ACA, 3.95 ns for 9ACA/Cu_2O, 3.06 ns for 9ACA/Cu_2O-rGO-0.25, 1.78 ns for 9ACA/Cu_2O-rGO-0.5, 1.69 ns for 9ACA/Cu_2O-rGO-1, 1.64 ns for 9ACA/Cu_2O-rGO-2, 2.68 ns for 9ACA/Cu_2O-rGO-5 and 3.12 ns for 9ACA/Cu_2O-rGO-10. Apparently, as the Cu_2O NCs and Cu_2O-rGO nanoheterostructures were dispersed in 9ACA solution, the PL lifetimes of 9ACA represented a decreasing behavior. In addition, the PL emission lifetimes of 9ACA/Cu_2O-rGO-x samples show a progressively decrease when the ingredient of rGO is increased. The PL lifetime decay of 9ACA in the 9ACA/Cu_2O and 9ACA/Cu_2O-rGO samples are thus mainly attributed to the charge transfer that occurred, leading to the suppression of radiative recombination. Cu_2O NCs can serve as an effective electron scavenger for 9ACA because its CB potential (−1.54 V vs NHE) is lower than the LUMO (Lowest Unoccupied Molecular Orbital) potential of 9ACA (−2.15 V vs NHE) as shown in Fig. 5(c). The photoexcited electrons on LUMO of 9ACA can inject into the CB of Cu_2O NC, resulting in depletion of the photoexcited electrons on LUMO of 9ACA and the subsequent suppression of the excitonic emission of 9ACA. Moreover, when 9ACA is mixed with Cu_2O-rGO sample, the photoexcited electrons on LUMO of 9ACA may further transfer into rGO through the Cu_2O-rGO interface due to the lower Fermi level potential (0 V vs NHE) of rGO as compared to the CB potential of Cu_2O NC. This two-step electron transfer facilitated the photoexcited electron depletion in 9ACA, resulting in the more pronounced PL emission decay of 9ACA in the 9ACA/Cu_2O-rGO-x samples.

Another possibility is that the direct injection of photoexcited electrons from LUMO of 9ACA into Fermi level of rGO may also contribute to the observed 9ACA emission depression of the 9ACA/Cu_2O-rGO-x samples as the gray arrow shown in Fig. 5(c). To clarify this issue, we further performed TRPL measurements to estimate the 9ACA emission lifetime in the presence of the rGO sheets. Note that the amount of rGO sheets relative to 9ACA was commensurate to the ingredient of rGO in the 9ACA/Cu_2O-rGO-x samples. As shown in Fig. 5(d), the PL lifetimes of 9ACA in the 9ACA/rGO samples were less quenched than the corresponding 9ACA/Cu_2O-rGO samples; however, the PL emission decays of 9ACA showed a progressively faster behavior as the rGO increased. Similarly, the PL lifetimes of 9ACA/rGO samples can also be fit with the double-exponential decay, and the obtained results were listed in Table 1. This result suggests that the photoexcited electron on LUMO of 9ACA can also inject into Fermi level of rGO but with an extent less pronounced than the electron injection into the CB of Cu_2O. This observation suggested that the electronic interactions between 9ACA and the rGO sheets were weaker than those between 9ACA and Cu_2O NCs, leading to the lower injection efficiency. Therefore, the significantly 9ACA emission decay of the 9ACA/Cu_2O-rGO-x samples is mainly contributed by the two-steps electron transfer from LUMO of 9ACA into CB of Cu_2O and further into Fermi level of rGO. The direct electron injection from LUMO of 9ACA into Fermi level of rGO is suggested to be the minor contribution to the overall situation.

3.6. The effect of Cu_2O NC decoration density for Cu_2O-rGO nanoheterostructures

The difference in the average PL lifetime of 9ACA between 9ACA/Cu_2O sample and the pure 9ACA indicates that there is a non-radiative pathway of charge carrier recombination due to the
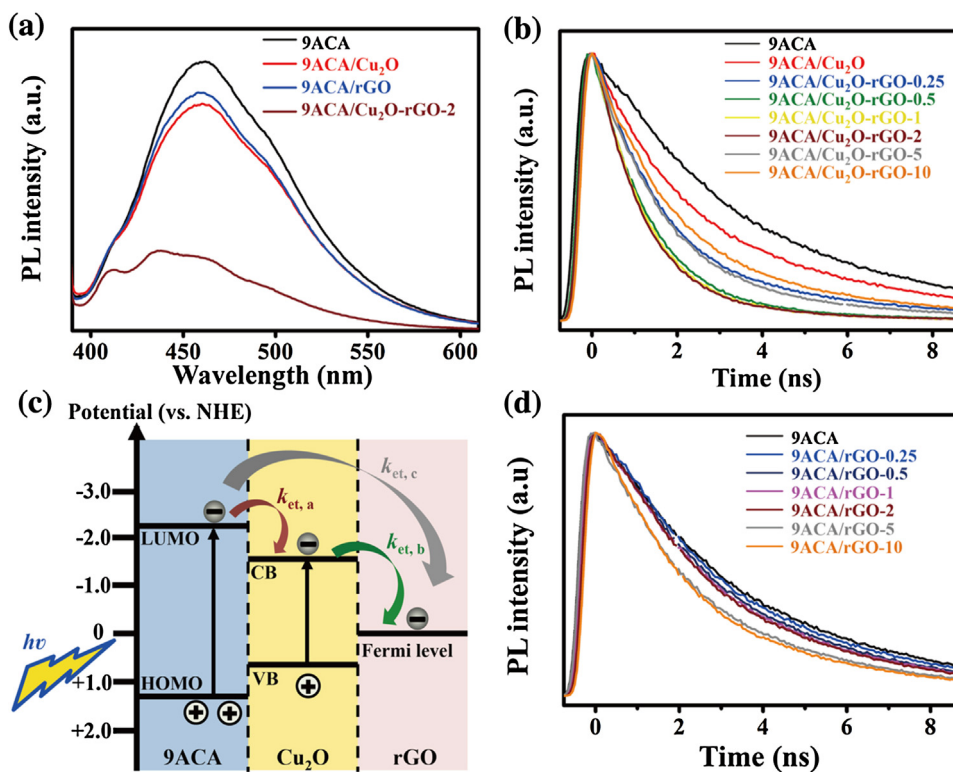
Fig. 5. (a) Steady-state PL spectra and (b) TRPL spectra of 9ACA in presence of Cu_2O and Cu_2O-rGO nanoheterostructure samples. (c) The energy diagrams of 9ACA, Cu_2O NCs and rGO. (b) TRPL spectra of 9ACA in presence of rGO samples.

Table 1
Kinetic analysis of PL decay for 9ACA in the presence of different samples.

entry (I)	$A_1/(A_1+A_2)$ (%)	τ_1 (ns)	$A_2/(A_1+A_2)$ (%)	τ_2 (ns)	$\langle\tau\rangle$ (ns)	χ^2	k_{et} (s⁻¹)
9ACA	43.3	2.35	56.7	4.99	4.29	2.35	
9ACA/Cu₂O	50.7	2.06	50.3	4.79	3.95	2.34	0.20×10^8 (9ACA → Cu₂O)[a]
9ACA/rGO-0.25	39.3	2.07	60.7	4.65	4.12	2.34	0.09×10^8 (9ACA → rGO-0.25)[c]
9ACA/rGO-0.5	44.7	2.05	55.3	4.46	3.81	2.35	0.30×10^8 (9ACA → rGO-0.5)[c]
9ACA/rGO-1	46.0	2.02	54.0	4.35	3.69	2.36	0.38×10^8 (9ACA → rGO-1)[c]
9ACA/rGO-2	47.7	1.97	52.3	4.30	3.61	2.37	0.44×10^8 (9ACA → rGO-2)[c]
9ACA/rGO-5	54.3	1.92	45.7	4.24	3.43	2.36	0.59×10^8 (9ACA → rGO-5)[c]
9ACA/rGO-10	56.4	1.75	43.6	4.22	3.35	2.38	0.65×10^8 (9ACA → rGO-10)[c]

entry (II)	$A_1/(A_1+A_2)$ (%)	τ_1 (ns)	$A_2/(A_1+A_2)$ (%)	τ_2 (ns)	$\langle\tau\rangle$ (ns)	χ^2	k_{et} (s⁻¹)
9ACA/Cu₂O-rGO-0.25	74.3	1.32	25.7	4.53	3.06	2.38	0.64×10^8 (Cu₂O → rGO-0.25)[b]
9ACA/Cu₂O-rGO-0.5	89.5	1.19	10.5	3.51	1.78	2.36	2.79×10^8 (Cu₂O → rGO-0.5)[b]
9ACA/Cu₂O-rGO-1	90.8	1.15	9.2	3.45	1.69	2.37	3.02×10^8 (Cu₂O → rGO-1)[b]
9ACA/Cu₂O-rGO-2	91.5	1.14	8.5	3.44	1.64	2.38	3.13×10^8 (Cu₂O → rGO-2)[b]
9ACA/Cu₂O-rGO-5	80.7	1.31	19.3	4.39	2.68	2.35	0.61×10^8 (Cu₂O → rGO-5)[b]
9ACA/Cu₂O-rGO-10	72.7	1.55	27.3	4.55	3.12	2.36	0.02×10^8 (Cu₂O → rGO-10)[b]

[a,c]The value was calculated using the expression
k_{et} (9ACA → A) $= \frac{1}{\tau}$ (9ACA/A) $- \frac{1}{\tau}$ (9ACA).
where A represents Cu₂O, rGO-0.25 wt.%, rGO-0.5 wt.%, rGO–1 wt.%, rGO–2 wt.%, rGO–5 wt.% and rGO–10 wt.% (wt.% relative to Cu₂O).
[b]The value was calculated using the expression
k_{et} (Cu₂O → rGO) $= \frac{1}{\tau}$ (9ACA/Cu₂O − rGO) $- \frac{1}{\tau}$ (9ACA/Cu₂O) $- k_{et}$ (9ACA → rGO).

electron transfer between 9ACA and Cu_2O NCs. The interfacial charge transfer from 9ACA to Cu_2O NCs would decrease the contribution of radiative recombination of 9ACA, resulting in the reduction of PL lifetime. This proposition can be confirmed by the emission quenching of 9ACA in the 9ACA/Cu_2O sample, which further validates the probe role of 9ACA in this work and its capability of injecting photoexcited electron from 9ACA into Cu_2O NCs. If electron transfer from 9ACA to Cu_2O was the predominant process that dictated the emission quenching of 9ACA for the 9ACA/Cu_2O sample, we can use the expression

$k_{et,a}$ (9ACA → Cu₂O) $= (1/\tau)$ (9ACA/Cu₂O) $- (1/\tau)$ (9ACA) to estimate an electron-transfer rate constant (k_{et}) of approximately 0.20×10^8 s⁻¹ [67,69–71]. Table 1 summarizes the k_{et} of the different processes that were calculated from the relevant samples. On the other hand, the PL lifetimes of 9ACA in the presence of the rGO sheets were 4.12 ns (9ACA/rGO-0.25), 3.81 ns (9ACA/rGO-0.50), 3.69 ns (9ACA/rGO-1), 3.61 ns (9ACA/rGO-2), 3.43 ns (9ACA/rGO-5) and 3.35 ns (9ACA/rGO-10), giving $k_{et,c}$ (9ACA → rGO) values of 0.09×10^8 s⁻¹, 0.30×10^8 s⁻¹, 0.38×10^8 s⁻¹, 0.44×10^8 s⁻¹, 0.59×10^8 s⁻¹ and 0.65×10^8 s⁻¹,

respectively. These values gradually increased as the constituent of the rGO sheets increased, verifying the corresponding electronic interactions of 9ACA with rGO sheets. By comparing the average lifetime of 9ACA for the 9ACA/Cu$_2$O-rGO-x and 9ACA/Cu$_2$O samples and deducting the contribution of electron transfer from 9ACA to rGO, we obtained $k_{et,b}$ (Cu$_2$O → rGO) values of 0.64×10^{-8} s^{-1} (9ACA/Cu$_2$O-rGO-0.25), 2.79×10^8 s^{-1} (9ACA/Cu$_2$O-rGO-0.5), 3.02×10^8 s^{-1} (9ACA/Cu$_2$O-rGO-1), 3.13×10^8 s^{-1} (9ACA/Cu$_2$O-rGO-2), 0.61×10^8 s^{-1} (9ACA/Cu$_2$O-rGO-5) and 0.02×10^8 s^{-1} (9ACA/Cu$_2$O-rGO-10). This result confirmed that rGO acted as an effective electron scavenger for Cu$_2$O NCs, leading to the pronounced charge separation of the Cu$_2$O-rGO nanoheterostructures, as revealed by the lower 9ACA PL lifetime. Meanwhile, the rGO in the present Cu$_2$O-rGO nanoheterostructures had a quantitative effect on the course of carrier transfer. As the rGO content of Cu$_2$O-rGO nanoheterostructures was increased from 0.25 to 2 wt.%, the $k_{et,b}$ showed a nearly 5 times increase from 0.64×10^{-8} to 3.13×10^{-8} s^{-1}, and the amplitude contribution of the fast decay (τ_1) showed a significant enhancement from 74.3 to 91.5%. This phenomenon indicates that controlling of the relative composition of Cu$_2$O-rGO nanoheterostructure can mediate its interfacial charge carrier dynamics. Furthermore, rGO of 2 wt.% represented the more significantly enhancement of $k_{et,b}$, indicating that rGO of 2.0 wt.% could attract more photoexcited electrons from Cu$_2$O, leading to the more pronounced charge carrier separation. However, the further increasing in the constituent of rGO to 5 and 10 wt.% in the Cu$_2$O-rGO nanoheterostructures caused a lower $k_{et,b}$ of 0.61×10^{-8} s^{-1} and 0.02×10^{-8} s^{-1}, respectively. This result suggests that the overall charge separation efficiency of the Cu$_2$O-rGO nanoheterostructures would be declined as the constituent of rGO exceeded 2 wt.%. It is generally believed that photoexcited electrons in a nanoheterostructure system can be attracted by the electron scavenger (metal or graphene) through the interface, resulting in the suppression of the electron-hole recombination [31,35,39,47,52,64,67]. However, the excess loading of the electron scavenger in nanoheterostructure would reduce the overall charge separation efficiency because of the consumption of the separated electrons in the later-emerging electron-hole recombination process [68,69]. In this regard, as the relatively high rGO content of 5 and 10 wt.% was present, the abundant electrons would be trapped at rGO sheets that may induce the significant electron-hole recombination across the Cu$_2$O/rGO interface. Consequently, the electron scavenging form Cu$_2$O was suppressed, resulting in the lengthened fast decay component (τ_1) with reduced amplitude contribution of 80.7 and 72.7% of Cu$_2$O-rGO-5 and Cu$_2$O-rGO-10. In addition, the charge recombination across the interface between Cu$_2$O and rGO may result in the additional quenching pathway which is an intrinsic long-lived state [69]. This effect can be confirmed by the prolonged lifetime of slow decay component and the increased amplitude contribution in Cu$_2$O-rGO-5 (τ_2 = 4.39 ns, 19.3%) and Cu$_2$O-rGO-10 (τ_2 = 4.55 ns, 27.3%). These result demonstrate that the excess rGO may play an interfacial charge-carrier recombination initiator to counteract the electron scavenging from Cu$_2$O as well as suppress the overall charge separation efficiency of Cu$_2$O-rGO nanoheterostructures.

3.7. Photocatalytic properties of Cu$_2$O NCs and Cu$_2$O-rGO nanoheterostructures

In order to assess the relation between the charge carrier dynamics and photoelectric conversion efficiency for Cu$_2$O-rGO nanoheterostructures, we further performed the photodegradation experiments by using MO as the probe molecule. A series of photocatalysis trials were executed to compare the ability of the Cu$_2$O NCs, rGO and Cu$_2$O-rGO nanoheterostructures samples to degrade MO under visible light illumination. The time-dependent absorption spectra of MO solutions under light illumination in the presence of Cu$_2$O-rGO were first shown in Fig. 6(a). The absorption spectra were composed of two bands in the wavelength range of 250–300 and 350–550 nm, which can be assigned to the electronic transitions at the phenyl and azo groups, respectively [86]. Upon light irradiation, these two bands were gradually depressed without shifting the spectra, suggesting that no intermediates were produced during the degradation process of MO [87]. Fig. 6(b) compares the photocatalytic performance of the as-prepared samples under visible light illumination. In the absence of a photocatalyst, MO showed almost no degradation, demonstrating its negligible self-photolysis under visible light illuminaton. After 120 min of irradiation, 84%, 92%, 93%, 98%, 71% and 60% of the MO were degraded by the Cu$_2$O-rGO-0.25, Cu$_2$O-rGO-0.5, Cu$_2$O-rGO-1, Cu$_2$O-rGO-2, Cu$_2$O-rGO-5 and Cu$_2$O-rGO-10, respectively. However, the Cu$_2$O NCs only degraded 51% of the MO, and the pure rGO sheets showed almost no photocatalytic activity under visible light illumination. Note that the quantity of rGO was the same as that in Cu$_2$O-rGO-2; therefore, the superior photocatalytic efficiency observed for the Cu$_2$O-rGO nanoheterostructure samples can be attributed to the effective interfacial charge separation between the Cu$_2$O NCs and the rGO sheets. Because the rGO sheets can scavenge the photoexcited electrons from CB and leave abundant holes in the VB of Cu$_2$O, the separated electrons and holes can be fully utilized for MO degradation. It should be noted that less than 5% of MO was adsorbed by Cu$_2$O and Cu$_2$O-rGO-2 in the dark, respectively, signifying that the dye adsorption contribution was fairly insignificant. Furthermore, the LUMO potential of MO has been reported as −3.27 eV vs. vacuum [88], which is lower than the CB potential of Cu$_2$O at −3.00 eV vs. vacuum [58]. This result suggested that the electron transfer from the excited MO to Cu$_2$O as well as the sensitization contribution from MO was improbable. To estimate the mineralization efficiency of MO, we further performed TOC analysis on MO solution by using Cu$_2$O-rGO-2 as the photocatalyst. The data were presented in the Supporting information. The results showed that almost complete mineralization of MO (mineralization efficiency = 91.4%) can be achieved upon 120 min of visible light irradiation, fairly close to the 98% of MO degradation efficiency observed in Fig. 6(b). This outcome illustrates that the results acquired from MO degradation efficiency were quantitatively consistent with the trends obtained from MO mineralization efficiency, which provided a reliable quantitative index to estimate the carrier utilization efficiency for the present Cu$_2$O-rGO nanoheterostructures. The photodegradation process can be further quantified by fitting the kinetic data to a pseudo-first-order reaction model [52,71]. The apparent rate constant of MO (k_{MO}) photodegradation can be determined by using the following expression: $\ln \left(\frac{C}{C_0} \right) = -k_{MO}t$, where C_0 and C are the concentrations of MO initially and at irradiation time, t, respectively, and k_{MO} is equal to the slope of the fitting line as shown in Fig. 6(c). Based on the fitting results, we obtained k_{MO} values of 0.0052 min^{-1}, 0.015 min^{-1}, 0.020 min^{-1}, 0.022 min^{-1}, 0.033 min^{-1}, 0.009 min^{-1} and 0.007 min^{-1} for Cu$_2$O NCs, Cu$_2$O-rGO-0.25, Cu$_2$O-rGO-0.5, Cu$_2$O-rGO-1, Cu$_2$O-rGO-2, Cu$_2$O-rGO-5 and Cu$_2$O-rGO-10, respectively. Obviously, the photocatalytic activity of the Cu$_2$O-rGO nanoheterostructures for MO photodegradation was higher than Cu$_2$O NCs. In addition, the increased k_{MO} of Cu$_2$O-rGO nanoheterostructures as the constituent of rGO increased from 0.25 to 2 wt.% was observed. The improvement of the photoactivity of Cu$_2$O-rGO nanoheterostructures mainly resulted from the deposited rGO sheets (content amount from 0.5–2 wt.%) which are able to promote the noticeable interfacial charge separation of Cu$_2$O NCs by readily attracting photoexcited electrons from the CB of Cu$_2$O to rGO, thereby providing a considerable amount of free electrons and holes to participate in MO degradation. However, the
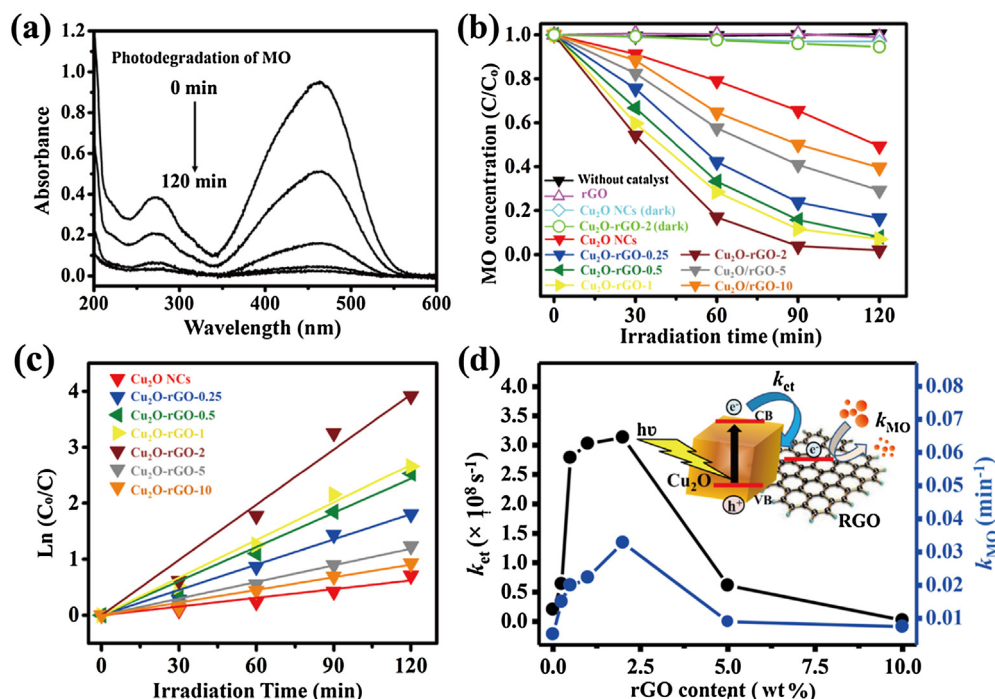
Fig. 6. (a) Absorption spectra of MO under different irradiation times by using Cu$_2$O-rGO-2 sample. (b) Plots of C/C$_0$ versus irradiation time for MO photodegradation without any catalyst and in the presence of Cu$_2$O, rGO, and Cu$_2$O-rGO nanoheterostructure samples. The results of MO adsorption by using Cu$_2$O and Cu$_2$O-rGO-2 in darkness were also included. (c) Ln(C$_0$/C) versus irradiation time plots with the fitting results included. (d) Correlations of the k_{et} and k_{MO} with the constituent of rGO sheets for Cu$_2$O-rGO nanoheterostructures.

k_{MO} of Cu$_2$O-rGO nanoheterostructures represented a decreased behavior when the content of rGO over to 5 and 10 wt.%, which may be due to the excessive rGO that provided the recombination centers to inhibit charge separation as mentioned in the earlier charge-carrier dynamics studies. It should be mentioned that the Cu$_2$O NCs and Cu$_2$O-rGO nanoheterostructure samples showed nearly identical MO adsorption capability. The Cu$_2$O NC and Cu$_2$O-rGO nanoheterostructure samples were incubated with MO as the mixed solutions in the dark for reaching the adsorption equilibrium before the visible light irradiation. After the incubation in the dark for 30 min, Cu$_2$O NCs, Cu$_2$O-rGO-0.25, Cu$_2$O-rGO-0.5, Cu$_2$O-rGO-1, Cu$_2$O-rGO-2, Cu$_2$O-rGO-5 and Cu$_2$O-rGO-10 adsorbed 15%, 11%, 13%, 16%, 14%, 12% and 15% of MO, respectively. This demonstration suggests that the observed enhancement of photocatalytic activity of Cu$_2$O-rGO nanoheterostructures was not related to the structure effect concerning surface area or dye adsorption, but derived from the difference of charge carrier dynamics modulated by the added amount of rGO. To clarify this relation, we plotted the correlation of the k_{et} and k_{MO} with the constituent of rGO for Cu$_2$O-rGO nanoheterostructures in Fig. 6(d). The correlation plot clearly represents the similar trend between k_{et} and k_{MO}, which further confirms that the composition of Cu$_2$O-rGO nanoheterostructure can affect its photocatalytic activity as well as modulate the interfacial charge carrier dynamics. In addition, the correlation plot concludes that an optimal composition for Cu$_2$O-rGO nanoheterostructures is Cu$_2$O-rGO-2, which has the highest interfacial charge transfer rate to achieve the most significantly charge separation for demonstrating the superior photocatalytic activity.

3.8. Photodegradation mechanism of MO by Cu$_2$O-rGO nanoheterostructures

In general, the degradation mechanism of dye molecule involves the scavenging of photoexcited electrons by the dissolved the O$_2$ in the reaction solution, thus forming the superoxide radical anion
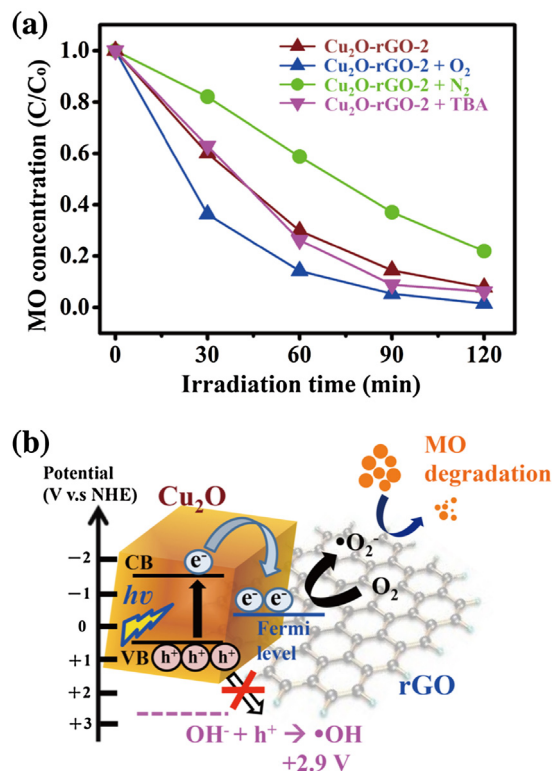
Fig. 7. (a) Plots of C/C$_0$ versus irradiation time for MO photodegradation in presence of Cu$_2$O-rGO-2 under different experimental conditions. (b) Scheme illustration of the band structure and relative potentials for Cu$_2$O-rGO nanoheterostructures toward to the formation of •O$_2$$^-$ and •OH radicals.

(•O$_2$$^-$) and hydrogen peroxide (H$_2$O$_2$) for further reacting with the dye [49]. On the other hand, the photoexcited holes can oxidize the
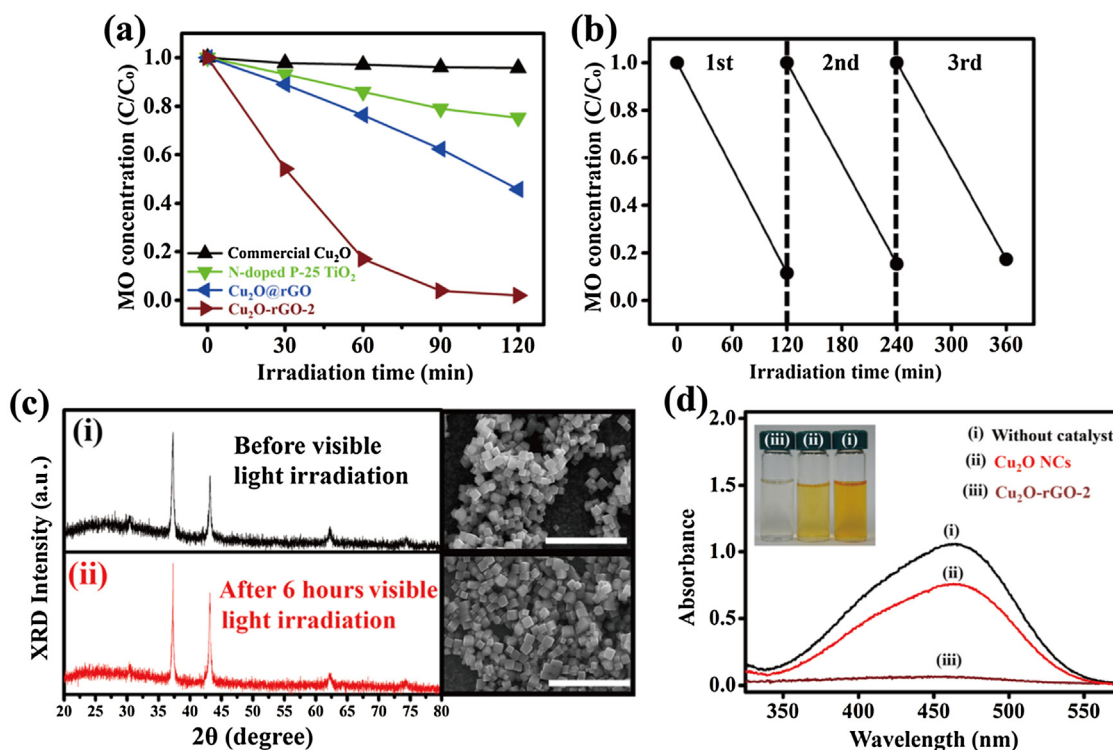
Fig. 8. (a) Plots of C/C_0 versus irradiation time for MO photodegradation in presence of four types of samples. (b) Recycling test of Cu_2O-rGO nanoheterostructures under visible light irradiation for three cycles of MO photodegradation. (c) XRD and SEM characterizations of Cu_2O (i) before and (ii) after 6 h of visble light irradiation. The scale bars of SEM images are 500 nm. (d) Absorption spectra of MO solutions after 4 h of exposure to daytime sunlight without any catalyst and in the presence of Cu_2O NCs and Cu_2O-rGO-2. Insets show the color of the corresponding solutions.

adsorbed water on the surface of photocatalyst to form ·OH, leading to the dye degradation [44]. To further clarify the photodegradation mechanism of MO in the present Cu_2O-rGO nanoheterostructures, we performed several control experiments by using Cu_2O-rGO-2 as the photocatalyst. As indicated by the results shown in Fig. 7(a), we examined the effects by the addition of an ·OH scavenger, *tert*-butyl alcohol (TBA), in the MO photocatalytic degradation [89]. There was no obvious effect on MO photodegradation, which indicates that the photogenerated holes of Cu_2O NCs and the subsequent ·OH radicals were the minor factor. In addition, the VB potential of Cu_2O is +0.6 V (vs. NHE), which doesn't exhibit enough oxidation ability to produce ·OH radicals (+2.9 V vs. NHE) as shown in Fig. 7(b). This result is also consistent with previous report about Cu_2O-rGO composition [58,61]. On the other hand, when the reaction solution was purged with O_2 and N_2 for ten minutes before the MO photocatalytic degradation, respectively, we observed a significantly difference in the photodegradation rate of MO. Interestingly, the MO photodegradation was abated under the N_2 purging, while the photodegradation rate of MO was slightly enhanced under the O_2 purging. Consequently, we can confirm that the dissolved O_2 in the reaction solution played a critical role in MO photodegradation for Cu_2O-rGO nanoheterostructures. The O_2 can scavenge the photoexcited electrons from the CB of Cu_2O to generate superoxide radical anions (·O_2^-) and hydrogen peroxide (H_2O_2) for the further degradation of MO. Furthermore, the reduction potential of $O_2/·O_2^-$ is −0.16 V (vs. NHE), which is very close to the Fermi level potential of rGO (~0 V vs. HNE) [37,42]. Consequently, the electron on the rGO surface could be captured by O_2 to form ·O_2^- and further generate H_2O_2. In addition, the rGO served a role to scavenge the photoexcited electron from Cu_2O, resulting in the abundant photoexcited electrons on rGO surface to promote the formation of ·O_2^- and H_2O_2 for MO degradation. Therefore, the scavenged electrons on rGO, as well as the radical anion process majorly dom-

inated the degradation mechanism of MO in the present Cu_2O-rGO nanoheterostructure.

3.9. Photocatalytic performance comparison and effect of recycling test

To further explore the applicability of the Cu_2O-rGO nanoheterostructures in a more practical situation, we performed MO photodegradation experiments using Cu_2O-rGO-2 under visible light irradiation and compared its performance with that of commercial Cu_2O powder, N-doped P25 TiO_2 powder, and Cu_2O@rGO (i.e., a physical mixture of Cu_2O NCs and rGO sheets with the same quantity of rGO sheets as that in Cu_2O-rGO-2). As shown in Fig. 8(a), superior photocatalytic efficiency was observed with Cu_2O-rGO-2. The commercial Cu_2O powder showed no photocatalytic activity, which indicates that the nanoscaled Cu_2O represents the superior photoactivity as compared to bulk or microscaled powder. In addition, the N-doped P25 TiO_2 just degraded 24% of MO under visible light irradiation, which demonstrates that the intrinsic low band gap of Cu_2O results in the better photon capture ability and thus displays better visible light photoactivity than N-doped P25 TiO_2. On the other hand, Cu_2O@rGO did not perform as well as Cu_2O-rGO-2 did (44% of MO was degraded by Cu_2O@rGO), presumably due to the destitute contact between Cu_2O NCs and the rGO sheets resulting in poor charge separation, thus leading to lower photoactivity. This result reaffirms the notable charge separation for Cu_2O-rGO nanoheterostructures, which is believed to occur at the interface, leading to the superior photocatalytic efficiency. In order to understand the recyclability and long-term stability for the further practical utilization of Cu_2O-rGO nanoheterostructures, we performed a recycling test of MO photodegradation by using Cu_2O-rGO-2 as the photocatalyst. As shown in Fig. 8(b), no appreciable decay of photocatalytic effi-

ciency was found for Cu_2O-rGO-2 after recycling in three rounds of MO photodegradation. To evaluate the stability during the photocatalytic process, the samples were characterized with XRD and SEM before and after 6 h of visible light irradiation. As evident from Fig. 8(c), no appreciable change in the crystal structure and morphology of Cu_2O can be observed, suggesting high chemical stability for Cu_2O-rGO. Moreover, the photocatalytic performance of Cu_2O-rGO nanoheterostructures under natural sunlight was also evaluated. In this experiment, two representative samples, Cu_2O NCs and Cu_2O-rGO-2, were tested and compared. As illustrated in Fig. 8(d), after 4 h of daytime sunlight exposure, the MO was totally degraded using Cu_2O-rGO-2, and this degradation was accompanied by an obvious decoloration of the resultant solution. In contrast, the Cu_2O NCs only decomposed 29% of MO under the same experimental condition. This difference, due to the remarkable charge separation property, occurred at the interface between the Cu_2O NCs and the rGO sheets. Most importantly, this result confirms that the present Cu_2O-rGO nanoheterostructures, especially Cu_2O-rGO-2, can indeed be used as a highly efficient visible light-driven photocatalyst for practical harvesting of energy from sunlight.

4. Conclusions

In conclusion, a facile and green photochemical reduction approach was developed to prepare Cu_2O-rGO nanoheterostructures. The decoration density of Cu_2O NCs on the rGO sheets was tunable by controlling the incorporated constituent of GO during synthesis. The interfacial charge carrier dynamics of the Cu_2O-rGO heterojunction system were investigated and presented. With a suitable amount of rGO, a fluent electron transfer from Cu_2O NCs to rGO sheets was achieved, giving rise to an increasingly pronounced charge separation in the samples. TRPL data showed an increased apparent electron transfer rate constant for Cu_2O-rGO nanoheterostructures, attributable to the capacity of the rGO sheets which captured photoexcited electrons from Cu_2O NCs to promote the overall charge separation efficiency. Furthermore, the charge transfer in the Cu_2O-rGO nanoheterostructures was characterized with a photocatalytic process under visible light illumination. The photocatalytic activity (k_{MO}) and interfacial charge transfer efficiency (k_{et}) were strongly depended on the constituent of rGO sheets, which demonstrated the critical role of rGO to medicate the interfacial charge carrier dynamics for Cu_2O-rGO nanoheterostructures. The photocatalytic activity of the Cu_2O-rGO nanoheterostructures was found to surpass that of pristine Cu_2O NCs, commercial Cu_2O powder and N-doped P-25 TiO_2 powder, presumably because of the superior charge separation property of the Cu_2O-rGO nanoheterostructure. By carrying out controlled experiments in the photocatalytic process, we confirmed that the photoexcited electron induced radical anions ($\bullet O_2^-$) and hydrogen peroxide (H_2O_2) were the major species for MO degradation. Furthermore, the Cu_2O-rGO nanoheterostructures retained comparable photocatalytic activities after repeated uses and recycling, revealing that their promise for utilization in a long-term course of photocatalysis. The performance evaluation under natural sunlight showed that the Cu_2O-rGO nanoheterostructures can be used as highly efficient photocatalysts for practical harvesting solar energy. The current work encourages one to further explore the coupling of semiconductor and graphene composites by using the suggested origins of the increasing charge separation as guidelines.

Acknowledgements

Appendix A. Supplementary data

Supplementary data associated with this article can be found, in the online version, at http://dx.doi.org/10.1016/j.apcatb.2016.11.012.

References

[1] K.S. Novoselov, A.K. Geim, S.V. Morozov, D. Jiang, Y. Zhang, S.V. Dubonos, V. Grigorieva, A.A. Firsov, Science 306 (2004) 666–669.
[2] K.S. Novoselov, V.I. Fal'ko, L. Colombo, P.R. Gellert, M.G. Schwab, K. Kim, Nature 490 (2012) 192–200.
[3] R.H. Baughman, A.A. Zakhidov, W.A. de Heer, Science 297 (2002) 787–792.
[4] H.W. Kroto, A.W. Allaf, S.P. Balm, Chem. Rev. 91 (1991) 1213–1235.
[5] S.V. Morozov, K.S. Novoselov, M.I. Katsnelson, F. Schedin, D.C. Elias, J.A. Jaszczak, A.K. Geim, Phys. Rev. Lett. 100 (2008) 016602.
[6] A.S. Mayorov, R.V. Gorbachev, S.V. Morozov, L. Britnell, R. Jalil, L.A. Ponomarenko, P. Blake, K.S. Novoselov, K. Watanabe, T. Taniguchi, A.K. Geim, Nano Lett. 11 (2011) 2396–2399.
[7] R.P. Ojha, P.A. Lemieux, P.K. Dixon, A.J. Liu, D.J. Durian, Nature 427 (2004) 521–523.
[8] A.K. Geim, Science 324 (2009) 1530–1534.
[9] A.A. Balandin, Nat. Mater. 10 (2011) 569–581.
[10] V. Barone, O. Hod, G.E. Scuseria, Nano Lett. 6 (2006) 2748–2754.
[11] D. Li, M.B. Muller, S. Gilje, R.B. Kaner, G.G. Wallace, Nat. Nanotechnol. 3 (2008) 101–105.
[12] F. Schwierz, Nature Nanotech. 5 (2010) 487–496.
[13] N. Cernetic, S. Wu, J.A. Davies, B.W. Krueger, D.O. Hutchins, X. Xu, H. Ma, A.K.Y. Jen, Adv. Funct. Mater. 24 (2014) 3464–3470.
[14] L. Britnell, R.V. Gorbachev, A.K. Geim, L.A. Ponomarenko, A. Mishchenko, M.T. Greenaway, T.M. Fromhold, K.S. Novoselov, L. Eaves, Nat. Commun. 4 (2013) 1794.
[15] W. Li, X. Geng, Y. Guo, J. Rong, Y. Gong, L. Wu, X. Zhang, P. Li, J. Xu, G. Cheng, M. Sun, L. Liu, ACS Nano 5 (2011) 6955–6961.
[16] M.G. Chung, D.H. Kim, H.M. Lee, T. Kim, J.H. Choi, D.k. Seo, J.-B. Yoo, S.-H. Hong, T.J. Kang, Y.H. Kim, Sens. Actuators B Chem. 166-167 (2012) 172–176.
[17] P. Li, B. Zhang, T. Cui, Biosens. Bioelectron. 72 (2015) 168–174.
[18] B. Seger, P.V. Kamat, J. Phys. Chem. C 113 (2009) 7990–7995.
[19] M. Liu, R. Zhang, W. Chen, Chem. Rev. 114 (2014) 5117–5160.
[20] L. Qu, Y. Liu, J.-B. Baek, L. Dai, ACS Nano 4 (2010) 1321–1326.
[21] Z.-S. Wu, W. Ren, L. Wen, L. Gao, J. Zhao, Z. Chen, G. Zhou, F. Li, H.-M. Cheng, ACS Nano 4 (2010) 3187–3194.
[22] H. Wang, L.-F. Cui, Y. Yang, H.S. Casalongue, T.J. Robinson, Y. Liang, Y. Cui, H. Dai, J. Am. Chem. Soc. 132 (2010) 13978–13980.
[23] J. Zhu, G. Zhang, X. Yu, Q. Li, B. Lu, Z. Xu, Nano Energy 3 (2014) 80–87.
[24] G. Ning, Z. Fan, G. Wang, J. Gao, W. Qian, F. Wei, Chem. Comm. 47 (2011) 5976–5978.
[25] J. Hou, Y. Shao, M.W. Ellis, R.B. Moore, B. Yi, Phys. Chem. Chem. Phys. 13 (2011) 15384–15402.
[26] F. Luan, G. Wang, Y. Ling, X. Lu, H. Wang, Y. Tong, X.X. Liu, Y. Li, Nanoscale 5 (2013) 7984–7990.
[27] J.J. Yoo, K. Balakrishnan, J. Huang, V. Meunier, B.G. Sumpter, A. Srivastava, M. Conway, A.L. Mohana Reddy, J. Yu, R. Vajtai, P.M. Ajayan, Nano Lett. 11 (2011) 1423–1427.
[28] X. Wang, L. Zhi, K. Mullen, Nano Lett. 8 (2008) 323–327.
[29] X. Miao, S. Tongay, M.K. Petterson, K. Berke, A.G. Rinzler, B.R. Appleton, A.F. Hebard, Nano Lett. 12 (2012) 2745–2750.
[30] Z. Yin, J. Zhu, Q. He, X. Cao, C. Tan, H. Chen, Q. Yan, H. Zhang, Adv. Energy Mater. 4 (2014), n/a-n/a.
[31] I.V. Lightcap, P.V. Kamat, Acc. Chem. Res. 46 (2013) 2235–2243.
[32] X. An, J.C. Yu, RSC Adv. 1 (2011) 1426.
[33] D. Chen, H. Zhang, Y. Liu, J. Li, Energy Environ. Sci. 6 (2013) 1362–1387.
[34] G. Xie, K. Zhang, B. Guo, Q. Liu, L. Fang, J.R. Gong, Adv. Mater. 25 (2013) 3820–3839.
[35] Q. Li, B. Guo, J. Yu, J. Ran, B. Zhang, H. Yan, J.R. Gong, J. Am. Chem. Soc. 133 (2011) 10878–10884.
[36] H. Li, Z. Xia, J. Chen, L. Lei, J. Xing, Appl. Catal. B: Environ. 168–169 (2015) 105–113.
[37] J.T. Wang, J.M. Ball, E.M. Barea, A. Abate, J.A. Alexander-Webber, J. Huang, M. Saliba, I. Mora-Sero, J. Bisquert, H.J. Snaith, R.J. Nicholas, Nano Lett. 14 (2014) 724–730.
[38] Q. Xiang, J. Yu, J. Phys. Chem. Lett. 4 (2013) 753–759.
[39] Y.-C. Chen, K. Katsumata, Y.-H. Chiu, K. Okada, N. Matsushita, Y.-J. Hsu, Appl. Catal. A: Gen. 490 (2015) 1–9.
[40] Q. Xiang, J. Yu, M. Jaroniec, Chem. Soc. Rev. 41 (2012) 782–796.
[41] K.-A. Tsai, Y.-J. Hsu, Appl. Catal. B: Environ. 164 (2015) 271–278.
[42] J. Zhang, J. Yu, M. Jaroniec, J.R. Gong, Nano Lett. 12 (2012) 4584–4589.

[43] S.K. Porter, K.G. Scheckel, C.A. Impellitteri, J.A. Ryan, Crit. Rev. Environ. Sci. Technol. 34 (2004) 495–604.
[44] Y. Zhang, Z.-R. Tang, X. Fu, Y.-J. Xu, ACS Nano 4 (2010) 7303–7314.
[45] Y. Zhang, N. Zhang, Z.R. Tang, Y.J. Xu, Phys. Chem. Chem. Phys. 14 (2012) 9167–9175.
[46] S.D. Perera, R.G. Mariano, K. Vu, N. Nour, O. Seitz, Y. Chabal, K.J. Balkus, ACS Catal. 2 (2012) 949–956.
[47] I.V. Lightcap, T.H. Kosel, P.V. Kamat, Nano Lett. 10 (2010) 577–583.
[48] N. Yang, Y. Liu, H. Wen, Z. Tang, H. Zhao, Y. Li, D. Wang, ACS Nano 7 (2013) 1504–1512.
[49] S. Malato, P. Fernández-Ibáñez, M.I. Maldonado, J. Blanco, W. Gernjak, Catal. Today 147 (2009) 1–59.
[50] Y.-C. Pu, Y. Ling, K.-D. Chang, C.-M. Liu, J.Z. Zhang, Y.-J. Hsu, Y. Li, J. Phys. Chem. C 118 (2014) 15086–15094.
[51] Y.C. Pu, G. Wang, K.D. Chang, Y. Ling, Y.K. Lin, B.C. Fitzmorris, C.M. Liu, X. Lu, Y. Tong, J.Z. Zhang, Y.J. Hsu, Y. Li, Nano Lett. 13 (2013) 3817–3823.
[52] Y.-C. Pu, Y.-C. Chen, Y.-J. Hsu, Appl. Catal. B: Environ. 97 (2010) 389–397.
[53] A. Mittiga, E. Salza, F. Sarto, M. Tucci, R. Vasanthi, Appl. Phys. Lett. 88 (2006) 163502.
[54] J.C. Park, J. Kim, H. Kwon, H. Song, Adv. Mater. 21 (2009) 803–807.
[55] F. Shao, J. Sun, L. Gao, J. Luo, Y. Liu, S. Yang, Adv. Funct. Mater. 22 (2012) 3907–3913.
[56] S. Sun, Nanoscale 7 (2015) 10850–10882.
[57] K. Tu, Q. Wang, A. Lu, L. Zhang, J. Phys. Chem. C 118 (2014) 7202–7210.
[58] Z. Gao, J. Liu, F. Xu, D. Wu, Z. Wu, K. Jiang, Solid State Sci. 14 (2012) 276–280.
[59] X. An, K. Li, J. Tang, ChemSusChem 7 (2014) 1086–1093.
[60] P.D. Tran, S.K. Batabyal, S.S. Pramana, J. Barber, L.H. Wong, S.C. Loo, Nanoscale 4 (2012) 3875–3878.
[61] W. Zou, L. Zhang, L. Liu, X. Wang, J. Sun, S. Wu, Y. Deng, C. Tang, F. Gao, L. Dong, Appl. Catal. B: Environ. 181 (2016) 495–503.
[62] L. Sun, G. Wang, R. Hao, D. Han, S. Cao, Appl. Sur. Sci. 358 (2015) 91–99.
[63] S.-H. Liu, Y.-S. Wei, J.-S. Lu, Chemosphere 154 (2016) 118–123.
[64] V. Chakrapani, K. Tvrdy, P.V. Kamat, J. Am. Chem. Soc. 132 (2010) 1228–1229.
[65] P.V. Kamat, Acc. Chem. Res. 45 (2012) 1906–1915.
[66] B. Luo, Y.-C. Pu, Y. Yang, S.A. Lindley, G. Abdelmageed, H. Ashry, Y. Li, X. Li, J.Z. Zhang, J. Phys. Chem. C 119 (2015) 26672–26682.
[67] T.-T. Yang, W.-T. Chen, Y.-J. Hsu, K.-H. Wei, T.-Y. Lin, T.-W. Lin, J. Phys. Chem. C 114 (2010) 11414–11420.
[68] Y.-C. Chen, Y.-C. Pu, Y.-J. Hsu, J. Phys. Chem. C 116 (2012) 2967–2975.
[69] Y.-F. Lin, Y.-J. Hsu, Appl. Catal. B: Environ. 130–131 (2013) 93–98.
[70] I.V. Lightcap, P.V. Kamat, J. Am. Chem. Soc. 134 (2012) 7109–7116.
[71] Y.-C. Pu, W.-H. Lin, Y.-J. Hsu, Appl. Catal. B: Environ. 163 (2015) 343–351.
[72] Y.C. Pu, M.G. Kibria, Z. Mi, J.Z. Zhang, J. Phys. Chem. Lett. 6 (2015) 2649–2656.
[73] M.G. Kibria, H.P.T. Nguyen, K. Cui, S. Zhao, D. Liu, H. Guo, M.L. Trudeau, S. Paradis, A.-R. Hakima, Z. Mi, ACS Nano 7 (2013) 7886–7893.
[74] W.S. HummersJr, R.E. Offeman, J. Am. Chem. Soc. 80 (1958) 1339.
[75] Y. Zhou, G. Chen, Y. Yu, L. Hao, Z. Han, Q. Yu, New J. Chem. 37 (2013) 2845–2850.
[76] C. Xu, X. Wang, L. Yang, Y. Wu, J. Solid State Chem. 182 (2009) 2486–2490.
[77] W.C. Huang, L.M. Lyu, Y.C. Yang, M.H. Huang, J. Am. Chem. Soc. 134 (2012) 1261–1267.
[78] Y. Matsumoto, M. Koinuma, S.Y. Kim, Y. Watanabe, T. Taniguchi, K. Hatakeyama, H. Tateishi, S. Ida, ACS Appl. Mater. Interfaces 2 (2010) 3461–3466.
[79] A.C. Ferrari, J. Robertson, J. Phys. Rev. B 61 (2000) 1126–1130.
[80] R.Y. Gengler, D.S. Badali, D. Zhang, K. Dimos, K. Spyrou, D. Gournis, R.J. Miller, Nat. Commun. 4 (2013) 2560.
[81] Y. Yang, Y. Ling, G. Wang, T. Liu, F. Wang, T. Zhai, Y. Tong, Y. Li, Nano Lett. 15 (2015) 7051–7057.
[82] J. Long, J. Dong, X. Wang, Z. Ding, Z. Zhang, L. Wu, Z. Li, X. Fu, J. Colloid Interface Sci. 333 (2009) 791–799.
[83] I. Martini, J.H. Hodak, G.V. Hartland, J. Phys. Chem. B 102 (1998) 9508–9517.
[84] I. Martini, J.H. Hodak, G.V. Hartland, J. Phys. Chem. B 103 (1999) 9104–9111.
[85] S. Lee, Sens. Actuators B 104 (2005) 35–42.
[86] A. Zyoud, A. Zu'bi, M.H. Helal, D. Park, G. Campet, H.S. Hilal, J. Environ. Health Sci. Eng. 13 (2015) 46.
[87] T. Chen, Y. Zheng, J.M. Lin, G. Chen, J. Am. Soc. Mass Spectrom. 19 (2008) 997–1003.
[88] X. Chang, M.A. Gondal, A.A. Al-Saadi, M.A. Ali, H. Shen, Q. Zhou, J. Zhang, M. Du, Y. Liu, G. Ji, J. Colloid Interface Sci. 377 (2012) 291–298.
[89] S.C. Yan, Z.S. Li, Z.G. Zou, Langmuir 26 (2010) 3894–3901.